

Measurement induced phase transitions in quantum raise and peel models

Eliot Heinrich¹ and Xiao Chen¹

¹Department of Physics, Boston College, 140 Commonwealth Avenue, Chestnut Hill, Massachusetts 02467, USA

(Dated: February 29, 2024)

We present a quantum circuit model which emulates the interface growth of the classical raise-and-peel model. Our model consists of Clifford unitary gates interspersed with projective measurements, applied according to prescribed feedback rules. We numerically find via large-scale simulations that, depending on the feedback rules, the system may undergo several measurement-induced entanglement transitions, including continuous transitions within a universality class not previously observed in hybrid random Clifford systems as well as a first-order transition.

INTRODUCTION

The past few years has witnessed the rapid development of quantum information dynamics, including the information scrambling and the emergent light cone behavior [1–11]. It is established that for many-qubit systems undergoing local unitary evolution, quantum systems tend towards highly entangled “volume-law” state, in which the entanglement entropy of a subsystem scales proportional to the volume of the subsystem.

Volume-law entanglement entropy scaling can be mitigated by interspersing the unitary evolution with projective measurements. Interestingly, when the measurement rate is low, a highly entangled volume-law phase persists. However, increasing the measurement rate induces a phase transition to a disentangled “area-law” phase, where the entanglement entropy of a subsystem scales proportionally to the boundary area. This phenomenon, known as the measurement-induced phase transition (MIPT), has been extensively studied, with the construction of numerous one-dimensional circuits to elucidate its underlying physics [12–20]. An intuitive conceptualization of this phase transition is offered through the surface growth picture, where the entanglement entropy, represented as a “height”, undergoes local increases via the application of a local unitary gate, while single-qubit measurements, on average, locally suppress the height [6, 11, 20, 21]. The competition between the two leads to the emergence of MIPT.

An example of a well studied classical surface growth model is the raise-and-peel model (RPM) [22, 23]. In the RPM, a substrate on a $1d$ lattice is updated by either locally depositing to the substrate or nonlocally “peeling” a layer, depending on the local configuration of the substrate. The RPM thereby has a *feedback* mechanism, wherein the configuration of the substrate affects dynamic updates applied in the immediate future. Analogously to the MIPT, this competition between adsorption and desorption leads to phase transition between a “flat” phase in which the average substrate height remains finite, and an “adsorbing” phase, in which the average substrate height is proportional to the system size. The RPM additionally has an intermediate phase between the

flat and adsorbing phases in which the substrate height scales algebraically with the system size, though slower than linear with the system size [22]. This intermediate phase is further characterized by long power-law tails in the sizes of avalanches, indicating that the intermediate phase is an example of self-organized criticality [23].

Building on the aforementioned research, this paper constructs a quantum entanglement entropy analogue to the RPM, replicating its feedback mechanism through non-unitary quantum dynamics. We focus on Clifford circuits, so that the entanglement entropy takes integer value in the logarithm base 2 and we are able to simulate the system for relatively large numbers of qubits. Application of local unitary gates emulates a strictly local surface deposition event, or a “raise” in the language of the RPM, while a projective measurement emulates a nonlocal “peel” update. We define a group of feedback modes which determine when a unitary/measurement gate should be applied. We find that the details of the feedback mode plays a very important role in the resulting phase diagram of the system. We identify three nontrivial phase diagrams, shown in Fig. 1, where two include continuous phase transitions representing a universality class not previously observed in hybrid Clifford systems. We also observe a first order transition for certain feedback modes.

MODEL DESCRIPTION

Consider a bipartition of a quantum state on a one-dimensional lattice of L qubits subject to open boundary conditions into subsystems A and B . The Renyi entanglement entropy of subsystem A is computed as

$$S_A^{(\alpha)} = \frac{1}{1-\alpha} \log_2 \text{Tr}(\rho_A^\alpha), \quad \rho_A = \text{Tr}_B(\rho) \quad (1)$$

where $\rho = |\psi\rangle\langle\psi|$ is the density matrix of the quantum state $|\psi\rangle$. For the remainder of this work, we will focus on stabilizer pure states [24], for which the Renyi entanglement entropy takes integer value and is independent of Renyi index α . We will drop the α from the notation. We will further restrict our interest to bipartitions in which

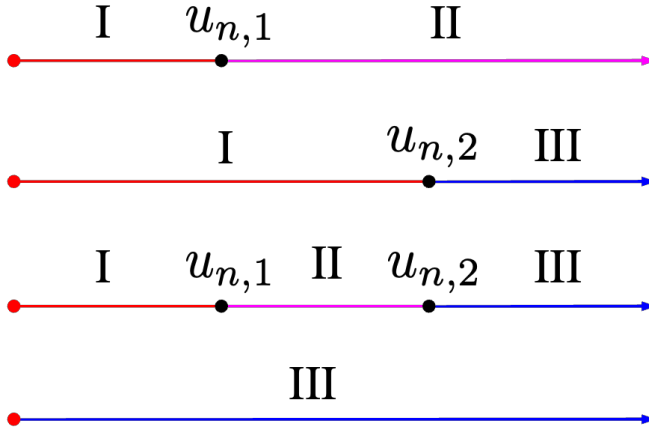


FIG. 1: The possible phase diagrams for the model in the text, depending on the feedback mode. The model parameter u increases from left to right. At $u = 0$, the entanglement entropy follows an area law regardless of the feedback mode, as no unitary operations occur. The area law (I) is indicated in red. In the first row, as u is increased, the system undergoes a continuous phase transition at $u = u_{n,1}$ into a volume law phase with fluctuations (II); this volume law is indicated in magenta. In the second row, the system instead undergoes a first-order transition at $u_{n,2}$ to a frozen volume law, characterized by vanishing fluctuations (III), indicated by blue. In the third row, the system undergoes both the continuous and first-order transitions, whereby II becomes an intermediate phase. Finally, in the last row, the system undergoes no phase transition, staying in the frozen volume law III for all $u > 0$.

A is a connected interval of qubits denoted $A = [a, b]$, where a (b) is the leftmost (rightmost) qubit of A . The entanglement entropy of this interval is denoted $S_{[a, b]}$. We define the entropy ‘‘substrate’’ height as $h_i = S_{[0, i]}$, where i is a site on the lattice dual to the qubit lattice, as shown in Fig. 2. Note that h_i automatically obeys the restricted solid-on-solid constraints typically enforced in interface growth models [25], as the entanglement entropy can change by at most 1 when a single qubit is added or removed to the interval, and $h_0 = h_L = 0$ by definition. As the states of interest are stabilizer states, the entanglement entropy profile is further restricted to change by $h_{i+1} - h_i \in \{-1, 0, 1\}$.

Acting on the entanglement substrate, we define update rules in the spirit of the RPM. For each discrete time step, a random site $j \in \{1, 2, \dots, L - 2\}$ is chosen. Based on the configuration of h_{j-1} , h_j , and h_{j+1} , either a four-qubit random Clifford gate, sampled using Ref. [26], or two single-qubit projective measurements may be applied. The local substrate configuration can be classified according to six possible (up to reflection) blocks, enumerated in Fig. 3. A feedback mode is defined as a set of

blocks for which a unitary gate is applied with probability p_u . For the remaining blocks, projective measurements in the Z basis are applied with probability p_m . At each timestep, a site is randomly chosen to be updated according to the feedback mode. The mode as well as the parameter $u = p_u/p_m$ determine the equilibrium behavior of the substrate. An example update step is indicated in Fig. 2.

Starting from the state $|0\rangle^{\otimes L}$ in which $h_i = 0$ for all i , it is clear any feedback rules which support non-trivial dynamics must apply a unitary to the (a) block, i.e. unitary gates must be applied to flat entropy substrates. Otherwise, we investigate all possible feedback modes. We find that this system, as a function of the feedback modes tabulated in Fig. 3 as well as the ratio $u = p_u/p_m$,

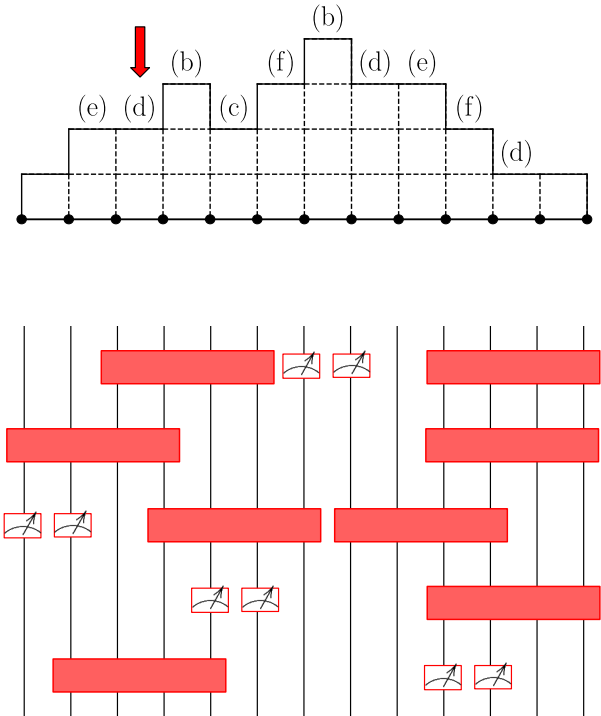


FIG. 2: The entropy substrate defined in the text. The top half of the figure show the entropy substrate h_i , with the blocks labelled. The qubits in the underlying quantum state are indicated with black circles. At each timestep, a site on the substrate is randomly selected; an example is indicated by the red arrow. Depending on the block observed, in this case (d), an update may be applied. If the observed block indicates a unitary operation, a four-qubit Clifford gate is applied to the four corresponding qubits with probability p_u . Otherwise, measurements in the Z basis are applied to the two corresponding qubits with probability p_m . In the bottom half of the figure, the corresponding quantum circuit evolution is displayed with commuting operations drawn as occurring at the same timestep.

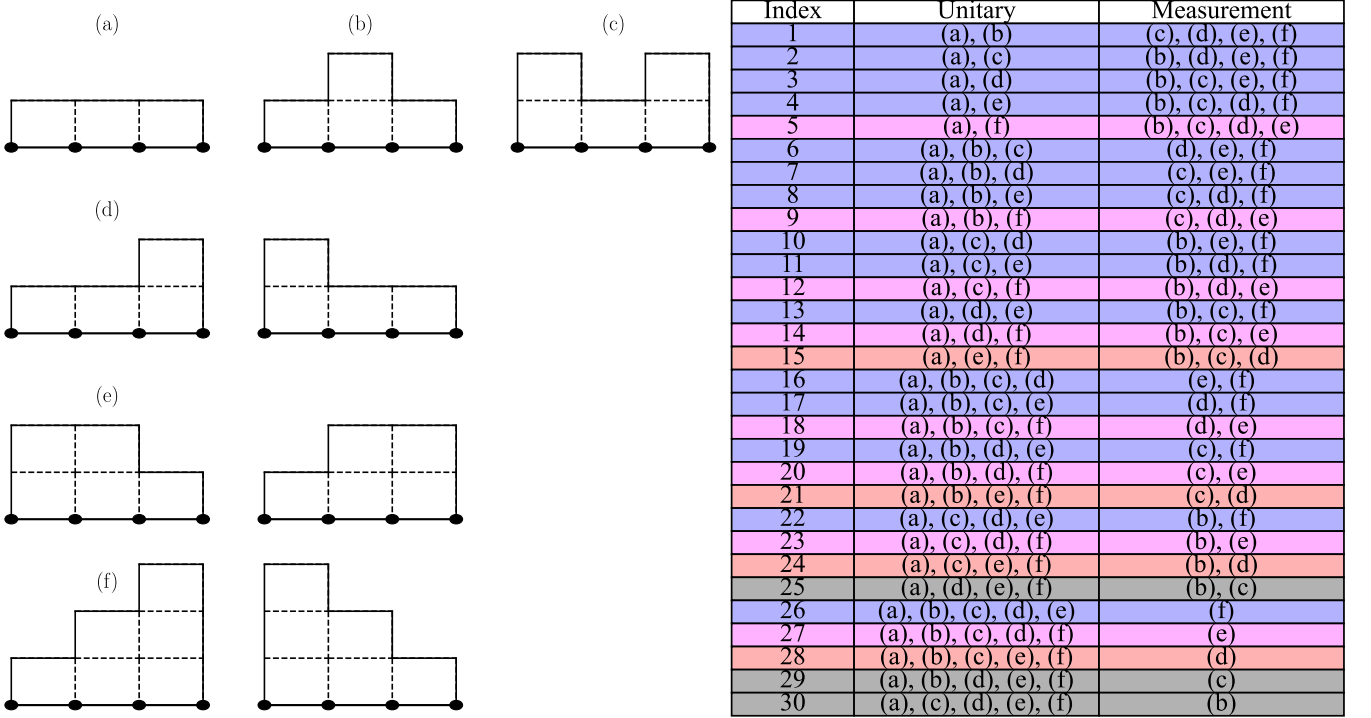


FIG. 3: On the left, the possible blocks specifying the local structure of the entropy substrate are labelled (a) through (f). The qubits corresponding to the entropy substrate are indicated as black dots on the bottom of the blocks. Note that (d), (e), and (f) each correspond to two distinct blocks which are equivalent under reflection, preserving directional symmetry in the substrate and feedback modes. On the right, each feedback mode considered is enumerated. The leftmost column labels the index used in the text to refer to the mode, the middle column lists the blocks for which a unitary gate is applied, and the rightmost column lists the blocks for which a projective measurement is applied. Note that unitaries are applied to (a) for all modes, since the entropy substrate of the initial system is entirely flat. The color of the columns indicate the classification of the modes according to phase transitions experienced, detailed in the text.

exhibits a rich variety of entanglement phases.

NUMERICAL RESULTS

For each feedback mode enumerated in Fig. 3, we examine the entanglement entropy as the parameter u is varied. For $u < 1$, we fix $p_m = 1$ and set $p_u = u$, and for $u > 1$, we fix $p_u = 1$ and set $p_m = 1/u$. We also compute the mutual information defined as

$$I_{AB} = S_A + S_B - S_{A \cup B} \quad (2)$$

for disjoint subsets of qubits A and B . The mutual information is a commonly-applied tool for diagnosing the existence of a phase transitions in monitored quantum dynamics; a sharp peak in the mutual information is typically associated with a measurement induced continuous phase transition[20]. Using the entanglement scaling and mutual information, we identify three distinct phases and four distinct groups of models, indicated by the row colors in Fig. 3. Data from the representative modes 10,

20, 21, and 30 for each of these four groups are displayed in Fig. 4 and Fig. 6. In addition, in the Appendix , we show the entropy substrate profile results for every feedback mode.

The first group consists of all modes which do not apply unitaries to the (f) blocks. These modes, represented by mode 10 in Fig. 4, exhibit a continuous phase transition at a mode-dependent $u_{n,1}$, where n indexes the mode, from area-law to volume-law entanglement scaling. Near the critical points, the entanglement entropy has logarithmic scaling in both space and time; that is, at early time $t \ll L$, the half-system entanglement scales as $S_{[0,L/2]} = \alpha_t \log t$ where we take the log to be base e if not otherwise specified, and, after equilibration, the entropy saturates and scales with subsystem size as $S_{[0,L_A]} \sim \alpha_s \log x$, where $x = \sin(\pi L_A/L)$. This logarithmic scaling is accompanied by a sharp peak in the mutual information, further indicating the presence of a critical point. The ratio of the scaling coefficients α_s and α_t is a universal quantity and equal to the dynamic critical exponent, i.e. $z = \alpha_s/\alpha_t$. We find that while

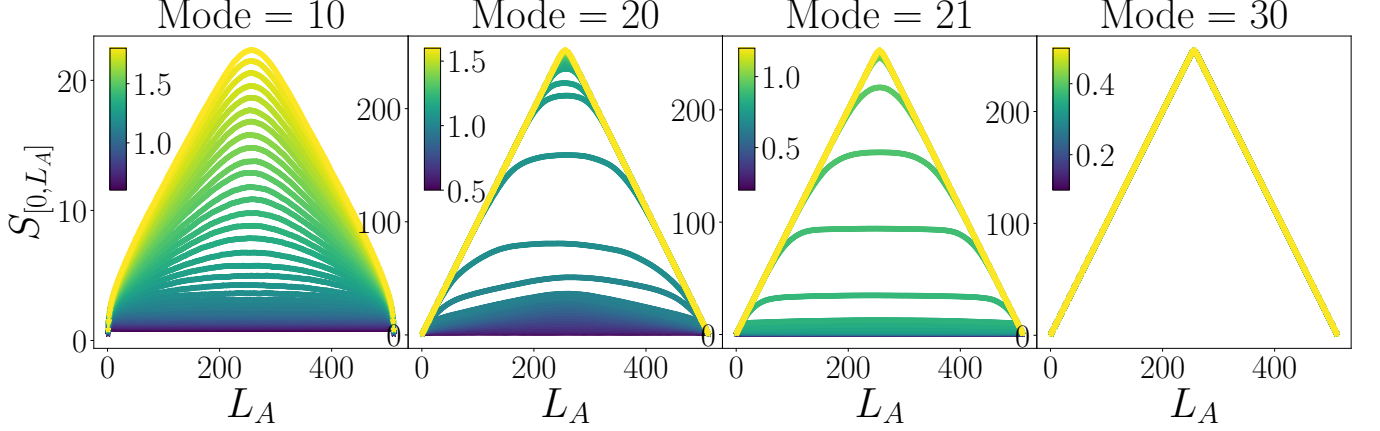


FIG. 4: The entropy substrate for a representative feedback mode from each group mentioned in the text. For modes 10, 20, 21, and 30, a system of $L = 512$ qubits is evolved starting from an initially unentangled state (except for mode 30, which starts from a fully entangled state) for $3000L$ steps to reach static equilibrium, followed by $2000L$ steps during which the entropy is sampled. We again average over 5 circuit realizations. The parameter u is selected uniformly on an interval $[u_{n,\min}, u_{n,\max}]$, with the purple lines corresponding to $u = u_{n,\min}$ and the yellow lines corresponding to $u = u_{n,\max}$. For mode 21, the curves lying between the area-law and volume-law scaling are near the transition point of the model, and we believe that they will be driven to either the volume-law or area-law in the thermodynamic limit; a finite-size scaling analysis is presented in Fig. 6.

z is close to 1, the scaling coefficients are different from the critical point of the hybrid random Clifford circuit, which manifests an emergent two-dimensional conformal symmetry [27]. Furthermore, we expect that the critical point is characterized by correlation lengths ξ_{\perp} and ξ_{\parallel} in the spatial and temporal directions respectively. They both diverge close to criticality as

$$\xi_{\perp} \sim (u - u_{n,1})^{-\nu_{\perp}}, \quad \xi_{\parallel} \sim (u - u_{n,1})^{-\nu_{\parallel}}. \quad (3)$$

We compute ν_{\perp} and ν_{\parallel} by identifying data collapses of the steady state entanglement entropy in the spatial direction

$$|S_{[0,LA]}(u) - S_{[0,LA]}(u_{n,1})| = (u - u_{n,1})^{\nu_{\perp}} L_A, \quad (4)$$

and of the early time entanglement growth

$$|S_{[0,L/2]}(t, u) - S_{[0,L/2]}(t, u_{n,1})| = (u - u_{n,1})^{\nu_{\parallel}} t, \quad (5)$$

for appropriately chosen ν_{\perp} and ν_{\parallel} . The dynamic exponent z can equivalently be calculated as $z = \nu_{\parallel}/\nu_{\perp}$; we find, by computing ν_{\perp} by searching for temporal data collapse and fitting $z = 1$, we get a good spatial data collapse, further indicating that $z = 1$. We show the space and time scaling of the entropy substrate as well as the data collapse for modes 10 and 20 in Fig. 8.

The volume-law phase exhibits significant fluctuations from one sample to another owing to the randomness present in the quantum circuits. Specifically, it is observed that for $t \ll L$, fluctuations along the temporal direction follow a power-law scaling form represented by

$$\delta S_{[0,L/2]}(t) = \sqrt{\langle [S_{[0,L/2]}(t)]^2 \rangle - \langle S_{[0,L/2]}(t) \rangle^2} \sim t^{\gamma} \quad (6)$$

where $\gamma = 1/3$ (See Fig. 5). These fluctuations are also observed in the volume-law phases of various random circuits and are indicative of the Kardar-Parisi-Zhang (KPZ) universality class, which characterizes a broad class of surface growth models [11, 28–32]. Furthermore, these fluctuations are observed in the entanglement entropy of the steady states, expressed as

$$\delta S_{[0,L/2]} = \sqrt{\langle [S_{[0,L/2]}]^2 \rangle - \langle S_{[0,L/2]} \rangle^2} \sim L^{\gamma}. \quad (7)$$

These fluctuations further contribute to a subleading correction in the steady state entanglement entropy with

$$S_{[0,L/2]} = a_1 L + a_2 L^{\gamma}. \quad (8)$$

We confirm this numerically in Fig. 5.

The second group, consisting of all modes which apply unitaries to the (e) and (f) block but not the (d) block (represented by mode 21 in Fig. 4), exhibits what appears to be a first-order transition in the half-system entanglement at the critical point $u_{n,2}$, as shown in the second column of Fig. 6. While this transition does seem to be an area-law to volume-law entanglement transition, we are unable to identify a critical point at which the entanglement follows the typical logarithmic scaling forms. Additionally, we note that as the parameter u is increased, the entanglement entropy density undergoes a rapid growth from 0 to 1. This becomes more pronounced and tends towards a step function as the system size is enlarged. This suggests that the volume-law phase exhibits almost maximal entanglement. We conclude that this transition is a first order entanglement transition, though we

note that there is a large peak in the mutual information at the transition point, which has also been observed in continuous phase transitions. We further note that the volume-law phase for these models is characterized by vanishing fluctuations except for near $L_A = L/2$, indicating that the volume-law phase is exceptionally stable; we show the fluctuations vanish beyond the transition point in Fig. 6. The stability of this maximally entangled volume-law phase can be understood by noting that

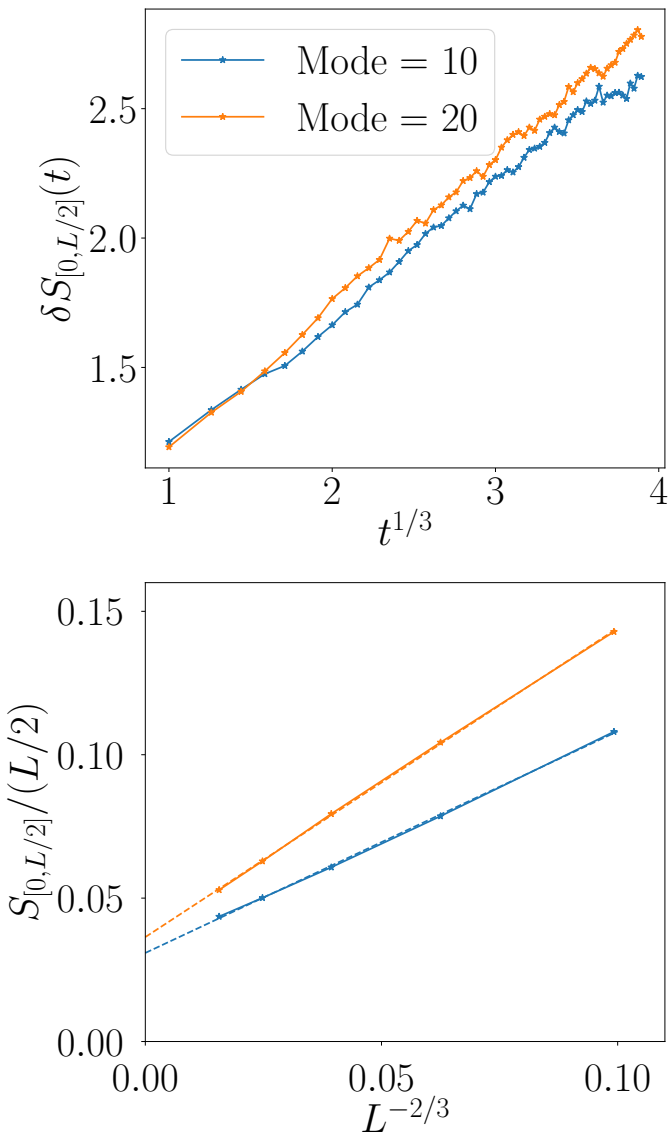


FIG. 5: We show the entanglement entropy density of modes 10 and 20 against $L^{-2/3}$ for $u = 1.8$ and $u = 0.89$, respectively, which lies within the volume-law of mode 10 and the intermediate volume-law of mode 20. The relationship is very close to linear, indicating that the volume-law phase of mode 10 and the intermediate phase of mode 20 both have volume-law entanglement scaling with KPZ fluctuations.

unitary gates are applied to the (f) block for these modes. A region of several contiguous (f) blocks, corresponding to a maximally entangled region of qubits, is fixed under the update rules of the model, as this region cannot be acted on by measurements except at the boundaries, and unitary gates cannot change the entropy without violating the solid-on-solid restrictions. Therefore, this region of (f) blocks becomes “frozen” when u is sufficiently large. This picture is illustrated in Fig. 7.

The third group, consisting of modes which apply a unitary to (f) but not (e), exhibits both of the above transitions. These modes, represented by mode 20 in Fig. 4 exhibit a continuous phase transition from an area-law entangled phase into an intermediate volume-law phase at $u_{n,1}$. At the critical point, the entropy scales close to logarithmically with respect to time and space, as in the first group of modes, although there are deviations from the logarithmic fit not observed in the first group; these can be seen in the third row of Fig. 8. Nonetheless, we are able to identify the scaling coefficients and critical exponents near the critical point, and find that modes 10 and 20 are distinct. These results are shown in Fig. 8. It’s worth noting that the intermediate volume-law phase also exhibits KPZ fluctuations, as confirmed by the numerical analysis presented in Fig. 5. As the parameter u is increased further, the system goes through a first order transition into the frozen volume-law phase described above at $u_{n,2}$. Both transitions are accompanied by peaks in the mutual information, although the peak associated with the second transition into the frozen volume-law phase is several orders of magnitude larger than the first peak, and this large difference makes the lower peak difficult to numerically resolve for small system sizes; we observe that the two peaks can be identified concretely when $L \sim 512$, as shown in Fig. 6.

The final group, consisting of modes which apply a unitary to all of (d), (e), and (f), appear to be drawn to the frozen maximally entangled volume-law phase independent of the parameter u . These systems have no entanglement transition at finite u . For very small u , the equilibration time becomes very large, so we instead start the system from a state which is close to maximally entangled and observe that the system is unable to de-scramble the information and reach an area-law for any u . This maximally entangled state is reached by operating $t \gg L$ layers of random two-qubit unitary Clifford gates. We note that the modes in the first three groups are all able to de-scramble initially maximally entangled states when u is small enough to leave the volume law.

Finally, to further connect our model to the classical RPM, we analyze a quantum entropy analogue of RPM avalanches. In particular, we compute the entropy “impact” of a measurement performed at time t , defined as

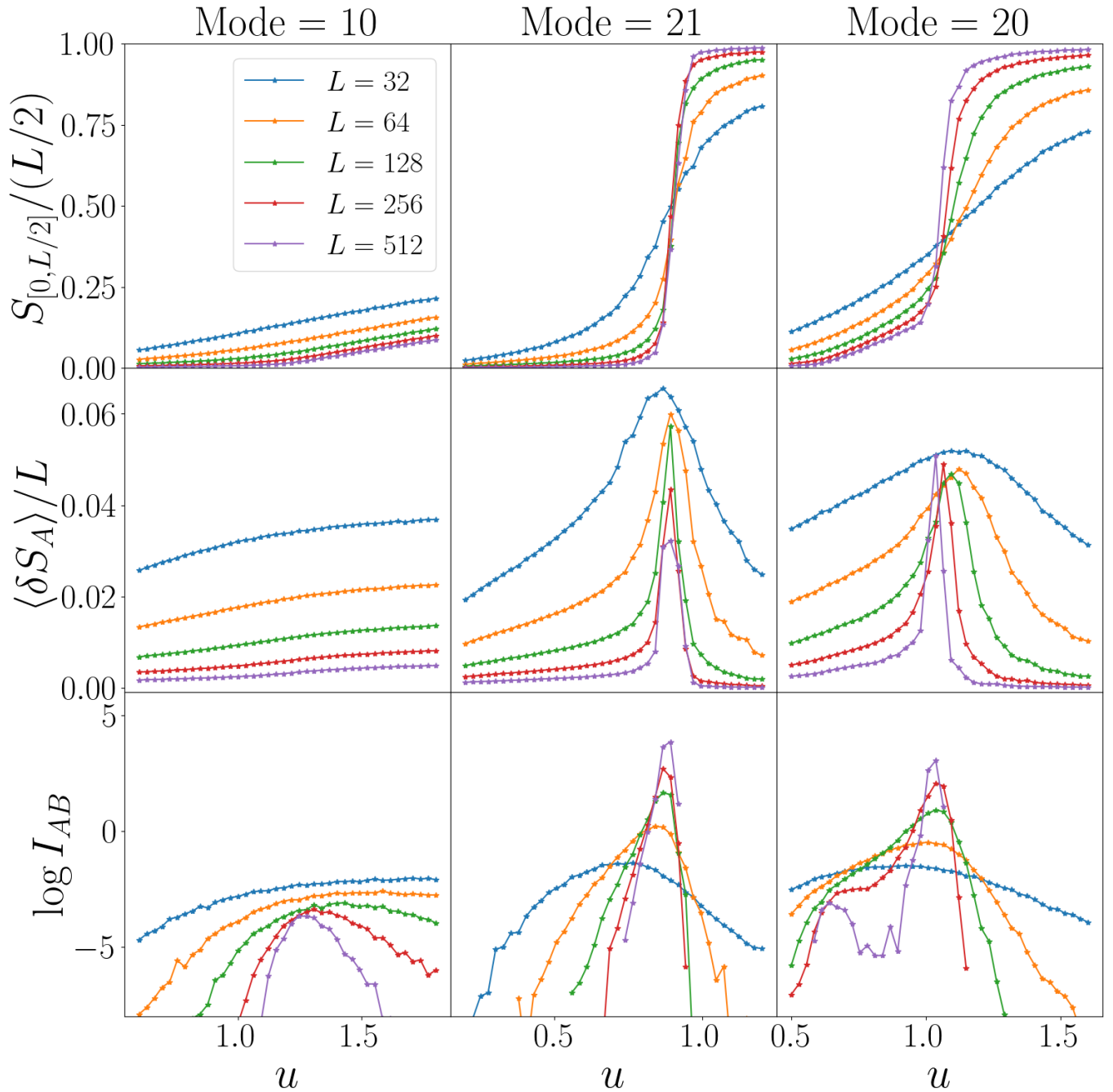


FIG. 6: Top: For varying u and L , the half-system entropy is plotted. For mode 10, the half-system entanglement changes continuously across the phase boundary around $u \approx 1.2$. Modes 20 and 21 exhibit discontinuous phase transitions in the half-system entanglement, indicated by the transition becoming increasingly sharp as the system size is increased. Middle: The entropy substrate fluctuations averaged over the entire profile. Entering the “frozen” volume law phase in modes 20 and 21, described in the text, the fluctuations become strong at the transition point before vanishing in the volume-law phase. Bottom: The natural logarithm of the mutual information for various system sizes is plotted. The subregions A (B) are chosen to be the $L/8$ leftmost (rightmost) qubits. Peaks which sharpen with increasing system size are visible for modes 10, 20, and 21, indicating the presence of entanglement transitions. An additional second peak is observed for mode 20 when L is sufficiently large ($L = 512$), indicating that the system undergoes a second transition as u is increased. We note that the magnitude of the peak near $u = 0.6$ is considerably smaller than the peak at $u = 1.0$, and is only visible by eye on a logarithmic scale.

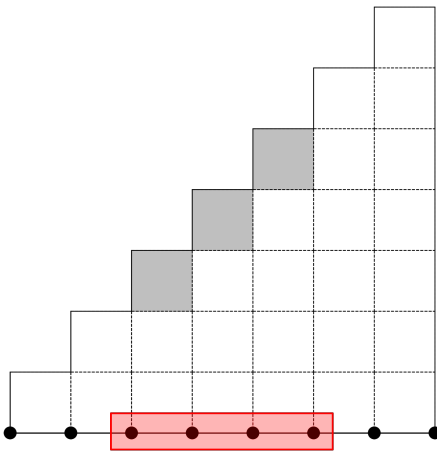


FIG. 7: We show an example of a substrate profile which, if the feedback mode under consideration applies four-qubit unitaries to the (f) block, becomes frozen into a maximally entangled configuration. The red box represents the region on which a four-qubit random Clifford gate is applied in our quantum hybrid model. The shaded blocks represent the area of the entropy substrate which can be affected by the local operation.

$$\sigma = \frac{1}{L} \sum_i \left[h_i^{(t+1)} - h_i^{(t)} \right] \quad (9)$$

$$= \frac{1}{L} \sum_i \left[S_{[0, L_i]}^{(t+1)} - S_{[0, L_i]}^{(t)} \right]. \quad (10)$$

Thus, if a measurement affects the global entropy substrate, $\sigma \rightarrow 1$, whereas if the measurement only locally affects the entropy substrate, $\sigma \rightarrow 0$. We show the results in Fig. 9. We find that the volume-law phase of mode 10 and the intermediate phase of mode 20 exhibit good fits to power-law behavior $P(\sigma) \sim \sigma^{\tau(u)}$ as characterized by the root mean square error

$$R = \sqrt{\frac{1}{L} \sum_{\sigma=1}^L (y(\sigma) - \hat{y}(\sigma))^2} \quad (11)$$

where $y(\sigma) = \log P(\sigma)$ and $\hat{y}(\sigma) = \tau\sigma + C$. The exponent τ depends on u and varies between $-3 < \tau(u) < -2$ for the regions where the fit is valid. A power-law distribution of this nature suggests that the local measurement has the capability to suppress the entanglement entropy within a substantial subsystem. Nevertheless, due to the fact that the ‘avalanche exponent’ $-\tau(u) > 2$, the measurement, on average, is only able to locally reduce entanglement. This power law behavior with large avalanche exponent has similarly been observed in the volume-law phase of the hybrid random Clifford circuit [20] and in the

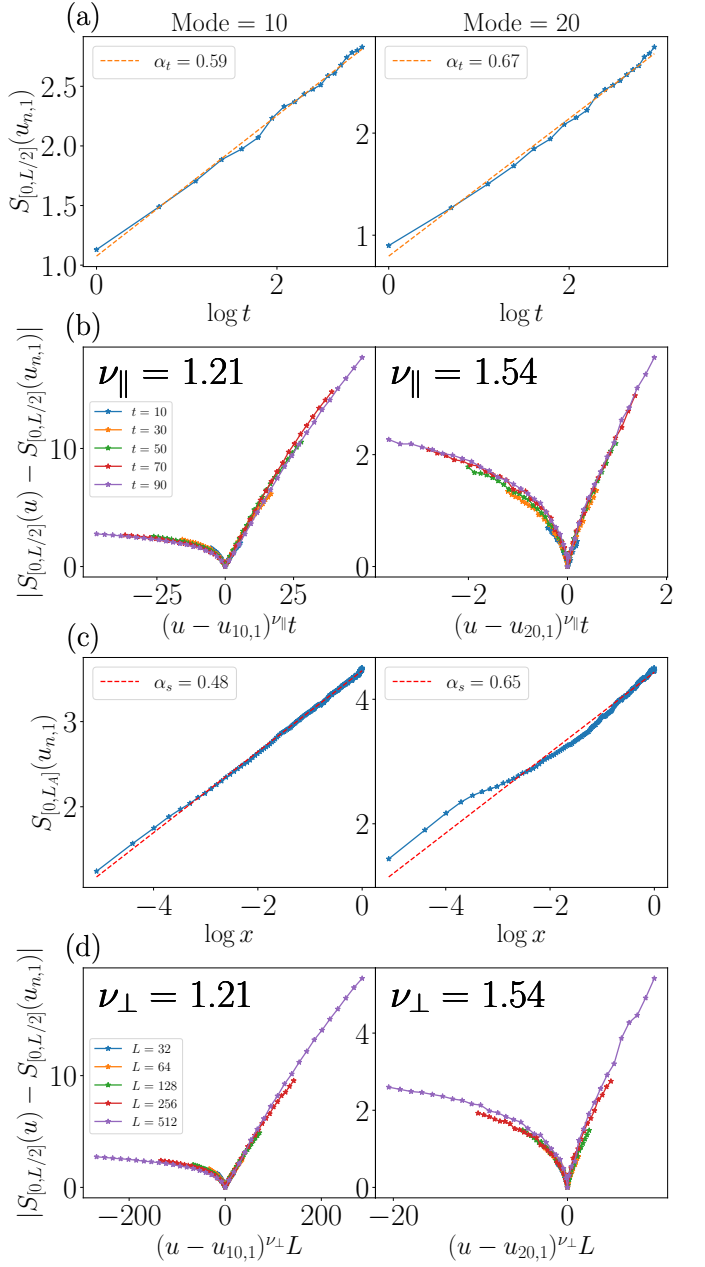


FIG. 8: (a) The half-system entanglement entropy before saturation is plotted against $\log t$ for feedback modes 10 and 20 at the critical points $u_{10} = 1.21$ and $u_{20} = 0.61$. (b) The temporal data collapse used to compute the critical exponent ν_{\parallel} for modes 10 and 20. For mode 20, only the region $u < u_{20,1}$ below the frozen volume law are considered in the data collapse. (c) The saturated entanglement entropy is plotted against $\log x$ at the critical points for modes 10 and 20. (d) The spatial data collapse for modes 10 and 20.

self-organized critical regime of the classical RPM [33]. Conversely, in the area-law and frozen volume-law phases of each model, the entropy impact is strictly local and

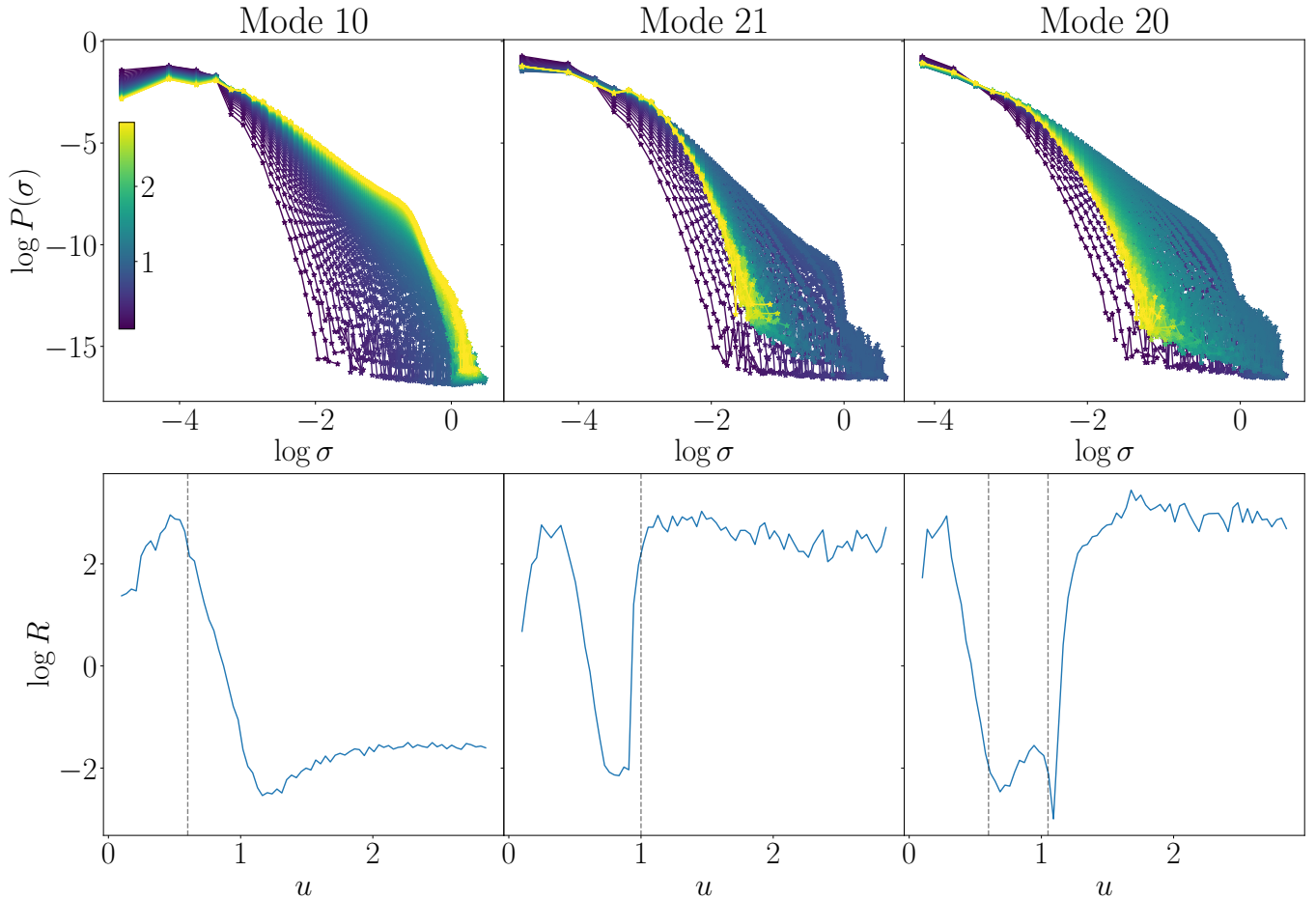


FIG. 9: Top: We show the entropy impact probability distribution for the three representative modes with phase transitions, with u indicated by the color of the line. Purple corresponds to $u = 0.2$ and yellow corresponds to $u = 5.0$, and the color is linearly interpolated in between. In the appropriate regime, described below and in the text, the distribution function is linear on the log-log scale, indicating power-law behavior. Bottom: We show the (logarithmic) least-squares error corresponding to the best-fit to the form $P(\sigma) = A\sigma^\tau$. We see that the error is small in the upper phase of mode 10 and the intermediate phase of mode 20. In the area-law phase of all three modes, the entanglement is finite, so the entropy impact will be local, resulting in a poor fit to power-law behavior. Likewise, in the frozen volume-law of modes 20 and 21, the system is experiencing very few measurements at the boundaries of the staircases which result in only locally affecting the entropy, again resulting in a poor fit to power-law behavior. Interestingly, for mode 21, despite transitioning directly from an area-law to a frozen volume-law, we see that for $u \lesssim u_{21}$, a power-law fit appears to have small error, indicating that the measurement impact becomes nonlocal only very near the transition point.

$P(\sigma)$ decays faster than polynomially, indicated by the downward curve in Fig. 9.

DISCUSSION AND CONCLUSION

In this work, we consider a $(1+1)d$ quantum hybrid circuit model consisting of random Clifford unitary gates and projective measurements. For each timestep, unitary gates or projective measurements are applied to a random site depending on the local configuration of the entanglement entropy substrate according to prescribed

feedback rules. This feedback mechanism, inspired by the RPM, leads to a rich phase diagram, shown in Fig. 1. We observe three distinct phases: the area-law phase, the volume-law phase with a subleading power law correction and the maximally entangled volume-law phase characterized by vanishing fluctuations. The presence of these phases are determined by the feedback mode. The phase transitions between the area-law phase and the volume-law phase with a correction term are continuous and are described universality classes distinct from those previously observed in hybrid Clifford circuits. Conversely, the phase transition to a maximally entangled frozen volume-

law phase is always a first-order transition. Our findings reveal that the critical exponents associated with the former transitions closely approximate $z = 1$. The frozen maximally entangled volume-law phase appears to act as a stable fixed point in the evolution for certain feedback models, resulting in a very stable configuration.

Furthermore, we compare our quantum model to the classical RPM by analyzing the distribution of avalanches, or, in the case of our model, the impact of measurements. We find that the effect of measurement on the entanglement substrate is local in the area-law phase and the maximally entangled volume-law phase, but for the volume-law phase with subleading correction term, measurements affect regions of the entropy substrate on all length scales, indicated by a power-law distribution. We find that the power-law exponent varies between -3 and -2, in agreement with the self-organized critical phase of the classical RPM. Additionally, this behavior is consistent with the volume-law phase of the hybrid random Clifford circuit.

ACKNOWLEDGEMENTS

We acknowledge computational support from the Boston College Andromeda cluster. This research is supported in part by the Google Research Scholar Program and is supported in part by the National Science Foundation under Grant No. DMR-2219735 (E. H. and X. C.).

- [1] S. H. Shenker and D. Stanford, JHEP **2015**, 1 (2015).
- [2] J. Maldacena, S. H. Shenker, and D. Stanford, JHEP **2016** (2016).
- [3] X. Chen and T. Zhou, Phys. Rev. B **100** (2019).
- [4] T. Zhou, S. Xu, X. Chen, A. Guo, and B. Swingle, Phys. Rev. Lett. **124**, 180601 (2020).
- [5] S. Xu and B. Swingle, Phys. Rev. X **9** (2019).
- [6] A. Nahum, S. Vijay, and J. Haah, Phys. Rev. X **8** (2018).
- [7] C. von Keyserlingk, T. Rakovszky, F. Pollmann, and S. Sondhi, Phys. Rev. X **8** (2018).
- [8] C.-F. Chen and A. Lucas, Phys. Rev. Lett. **123** (2019).
- [9] M. C. Tran, A. Y. Guo, Y. Su, J. R. Garrison, Z. Eldredge, M. Foss-Feig, A. M. Childs, and A. V. Gorshkov, Phys. Rev. X **9** (2019).
- [10] N. Lashkari, D. Stanford, M. Hastings, T. Osborne, and P. Hayden, JHEP **2013** (2013).

- [11] A. Nahum, J. Ruhman, S. Vijay, and J. Haah, Phys. Rev. X **7** (2017).
- [12] B. Skinner, J. Ruhman, and A. Nahum, Phys. Rev. X **9**, 031009 (2019).
- [13] Y. Li, X. Chen, and M. P. A. Fisher, Phys. Rev. B **98**, 205136 (2018).
- [14] A. Chan, R. M. Nandkishore, M. Pretko, and G. Smith, Phys. Rev. B **99**, 224307 (2019).
- [15] J. M. Koh, S.-N. Sun, M. Motta, and A. J. Minnich, Nat. Phys. **19**, 1314–1319 (2023).
- [16] A. Zabalo, M. J. Gullans, J. H. Wilson, R. Vasseur, A. W. W. Ludwig, S. Gopalakrishnan, D. A. Huse, and J. H. Pixley, Phys. Rev. Lett. **128**, 050602 (2022).
- [17] J. Iaconis, A. Lucas, and X. Chen, Phys. Rev. B **102** (2020).
- [18] S. Choi, Y. Bao, X.-L. Qi, and E. Altman, Phys. Rev. Lett. **125**, 030505 (2020).
- [19] M. J. Gullans and D. A. Huse, Phys. Rev. X **10** (2020).
- [20] Y. Li, X. Chen, and M. P. A. Fisher, Phys. Rev. B **100** (2019).
- [21] R. Morral-Yepes, A. Smith, S. Sondhi, and F. Pollmann, PRX Quantum **5**, 010309 (2024).
- [22] J. de Gier, B. Nienhuis, P. A. Pearce, and V. Rittenberg, J. Stat. Phys **114**, 1 (2004).
- [23] D. A. C. Jara and F. C. Alcaraz, J. Stat. Mech. Theory Exp. **2018**, 053205 (2018).
- [24] S. Aaronson and D. Gottesman, Phys. Rev. A **70** (2004).
- [25] J. M. Kim and J. M. Kosterlitz, Phys. Rev. Lett. **62**, 2289–2292 (1989).
- [26] E. V. D. Berg, in *2021 IEEE International Conference on Quantum Computing and Engineering (QCE)* (IEEE Computer Society, Los Alamitos, CA, USA, 2021) pp. 54–59.
- [27] Y. Li, X. Chen, A. W. W. Ludwig, and M. P. A. Fisher, Phys. Rev. B **104** (2021).
- [28] M. Kardar, G. Parisi, and Y.-C. Zhang, Phys. Rev. Lett. **56**, 889 (1986).
- [29] I. Corwin, Random Matrices: Theory Appl. **01**, 1130001 (2012).
- [30] Y. Li, S. Vijay, and M. P. Fisher, PRX Quantum **4** (2023).
- [31] Y. Han and X. Chen, Phys. Rev. B **107**, 014306 (2023).
- [32] T. Zhou and A. Nahum, Phys. Rev. B **99** (2019).
- [33] F. C. Alcaraz, E. Levine, and V. Rittenberg, J. Stat. Mech. Theory Exp. **2006**, P08003–P08003 (2006).

Results for all modes

In this section, we show results for the entropy scaling for every mode enumerated in Fig. 3. These results are displayed in Fig. 10

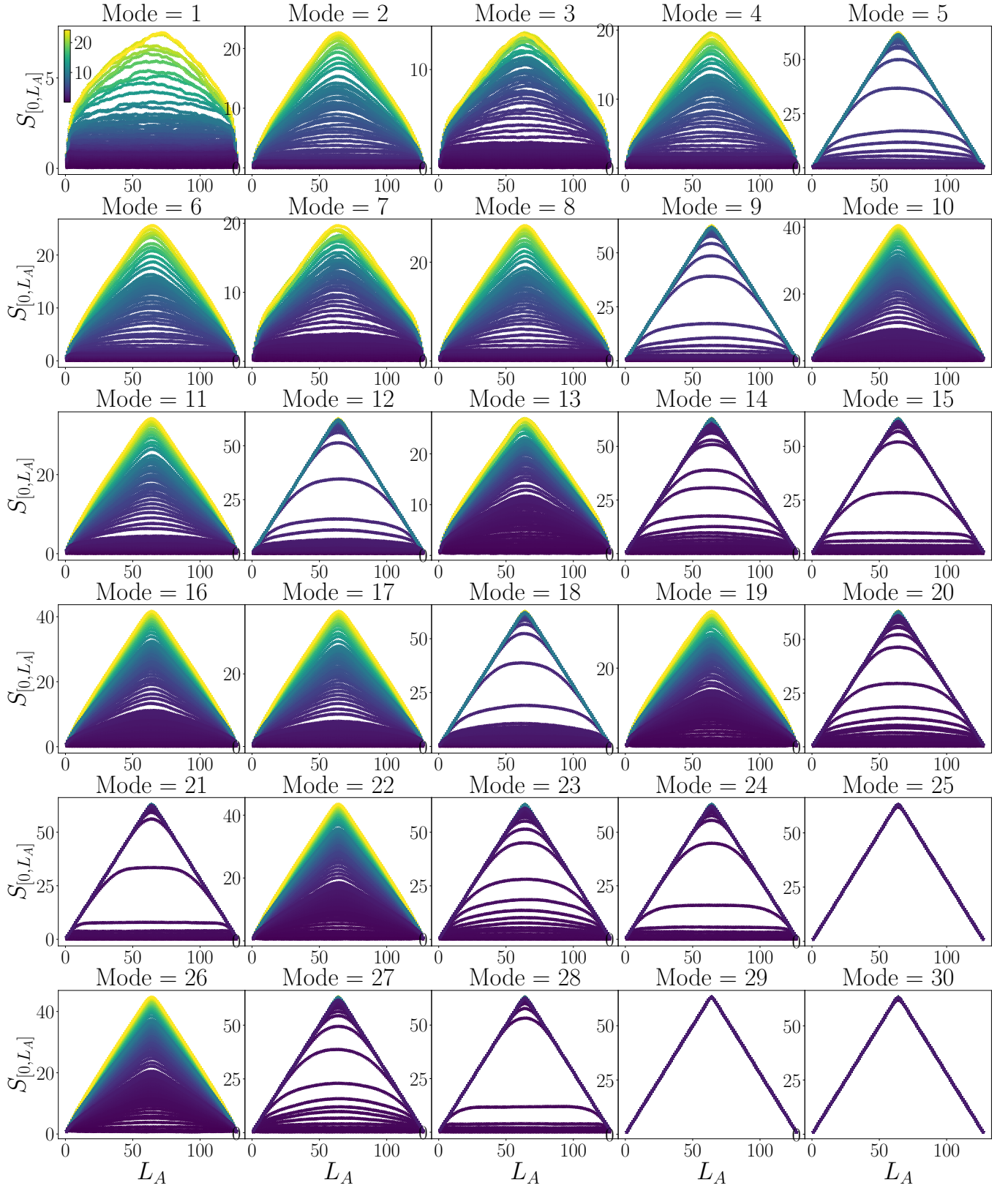


FIG. 10: We show the entanglement scaling for all modes. For each mode, we choose $L = 128$ and evolve the system for $t = 3000L$ timesteps followed by $2000L$ timesteps of sampling. We average over 5 repetitions of this evolution.